Re-Engineering and Evaluation of Anti-DNA Autoantibody 3E10 for Therapeutic Applications

Zahra Rattray,[a*] *Valentina Dubljevic,*[b] *Nicholas J.W. Rattray,*[c] *Deanne L. Greenwood,*[b] *Caroline H. Johnson,*[c] *James A. Campbell,*[b] *and James E. Hansen* [a,d*]

a. Department of Therapeutic Radiology, Yale School of Medicine, Yale University, New Haven, CT, USA.
b. Patrys Ltd, Melbourne, Australia.
c. Department of Environmental Health Sciences, Yale School of Public Health, Yale University, New Haven, CT, USA.
d. Yale Cancer Center, New Haven, CT, USA.

*Corresponding authors: Zahra Rattray (zahra.rattray@yale.edu), James E. Hansen (james.e.hansen@yale.edu)

ABSTRACT

A key challenge in the development of novel chemotherapeutics is the design of molecules capable of selective toxicity to cancer cells. Antibodies have greater target specificity compared to small molecule drugs, but most are unable to penetrate cells, and predominantly target extracellular antigens. A nuclear-penetrating anti-DNA autoantibody isolated from the MRL/lpr lupus mouse model, 3E10, preferentially localizes to tumors, inhibits DNA repair, and selectively kills cancer cells with defects in DNA repair. A murine divalent single chain variable fragment of 3E10 with mutations for improved DNA binding affinity, 3E10 (D31N) di-scFv, has previously been produced in P. pastoris and yielded promising pre-clinical findings, but is unsuitable for clinical testing. The present study reports the design, expression and testing of a panel of humanized 3E10 (D31N) di-scFvs, some of which contain CDR substitution. These variants were expressed in a modified CHO system and evaluated for their physicochemical attributes and ability to penetrate nuclei to selectively cause DNA damage accumulation in and kill cancer cells with DNA repair defects. Secondary structure was conserved and most variants retained the key characteristics of the murine 3E10 (D31N) di-scFv produced in P. pastoris. Moreover, several variants with CDR substitutions outperformed the murine prototype. In conclusion, we have designed several humanized variants of 3E10 (D31N) di-scFv that have potential for application as monotherapy or conjugates for targeted nuclear drug delivery.

KEYWORDS 3E10; di-scFv; autoantibody; DNA damage repair; synthetic lethality

1. Introduction

Challenges associated with the low therapeutic index and associated off-target toxicity of small molecule chemotherapy drugs has given rise to an ever-expanding portfolio of antibodies targeted against cancer antigens. The past decade has seen an exponential growth of antibodies used in the treatment of malignancies, and more recently, with gains in linker chemistry and an understanding of antibody properties, antibody-drug conjugates [1] have emerged as a viable platform to improve chemotherapeutic outcomes. While such antibody therapeutics have been successful, their utility in targeting intracellular antigens has been limited due to their inability to directly penetrate cells and access intracellular compartments [2]. Hence, most antibodies in clinical development are against extracellular target antigens [3].

Autoantibodies reactive to intracellular host antigens are associated with inflammation and poor prognosis in autoimmune diseases [4, 5]. Most cell-penetrating autoantibodies are toxic, but 3E10, an anti-DNA autoantibody isolated from the MRL/lpr lupus mouse model, has been found to penetrate nuclei in a manner that is non-toxic to normal cells [6]. 3E10 inhibits DNA single and double-strand break (DSB) repair and is synthetically lethal to cancer cells defective in DNA repair machinery (e.g. BRCA1/2 and PTEN mutations), but spares DNA repair-proficient cells [7, 8]. Additionally, 3E10 is attracted to DNA released by necrotic cancer cells, and preferentially accumulates at tumor sites *in vivo* suggesting its use in cancer therapy [7].

Previously a divalent 3E10 single chain variable fragment with improved DNA binding affinity (3E10 (D31N) di-scFv), hereafter referred to as di-scFv was evaluated [9]. Di-scFv lacks the unnecessary 3E10 Fc region that has potential to contribute to non-specific toxicity. Di-scFv has yielded promising pre-clinical results both as a monotherapy against DNA repair-deficient

tumors and as a drug delivery ligand [9, 10], but due to C-terminal Myc and His6 tags is unsuitable for human use. Herein, we report the design, expression and evaluation of a panel of novel humanized di-scFv variants that lack any tags with a view to utilizing them as novel anticancer agents or drug delivery ligands.

2. Material and Methods

2.1. Reagents

Unless otherwise stated, all cell culture reagents, protein L, and primary and secondary antibodies were obtained from Invitrogen (Carlsbad, CA, USA).

2.2. In silico humanization of di-scFv

Murine di-scFv with C-terminal Myc and His6 tags was previously designed and evaluated using a combination of *in vitro* and *in vivo* studies [9]. Di-scFv lacks an Fc, and therefore efforts to humanize di-scFv focused on VL and VH domains. Sequence alignments between the murine di-scFv VL and VH, and human germline sequences identified the optimal acceptor framework for di-scFv VL and VH. J-segments were also selected. *In silico* CDR-grafting was subsequently performed wherein amino acids in the di-scFv framework sequence were changed to that of the human sequence. Subsequently, a series of back-mutations were selected to maintain di-scFv function by preserving the VL-VH interface and Vernier zone. Following completion of CDR-grafting and selection of back-mutations, the resulting sequences were immunoprofiled against 85 HLA class II allotypes to identify Th epitopes. Sequences were also screened for potential post-translational modification (PTM) sites. In some cases, substitutions within CDRs were permitted to reduce immunogenicity and screen for effects on cellular penetration. Ultimately, a panel of six distinct humanized VL (three containing a CDR change, and three without CDR

changes) and six VH (three containing a CDR change and three without CDR changes) were selected, and 16 different combinations of these fragments were selected for expression (supplementary information Table S1).

2.3. Protein expression & purification

The murine (yeast) di-scFv prototype was expressed in *P. pastoris* and purified using approaches described elsewhere [9]. For novel di-scFv prototype expression, cDNAs encoding the murine di-scFv sequence or each of the 16 humanized variants were synthesized and sub-cloned into a proprietary CHO expression vector. Stable CHO cell pools expressing the antibody fragments were generated in CD-CHO media (Invitrogen) and a base feed utilized for the expression culture (bolus feed was added on day four, and the cultures harvested at day eight). The medium was subsequently centrifuged to remove cellular matter, and filtered using a 0.22 µm pore-sized filter. Purification of di-scFv variants was achieved using a two-step process including ion exchange chromatography and NaCl gradient elution (over 20 column volumes) on an Äkta system equipped with a HiTrap Capto S column at a (5 mL/min flow rate) (GE Healthcare). Following purification, samples were concentrated using Amicon Ultra-15 filters (Millipore) and subjected to analysis of monomeric purity using SEC-HPLC (see supplementary information, **Table S2**).

2.4. Cell lines

A matched pair of isogenic BRCA2-proficient and -deficient DLD-1 colon cancer cells (Horizon Discovery Ltd) were grown in RPMI-1640 supplemented with 10% *v/v* FBS. PTEN-deficient U251 and PTEN-proficient U251-PTEN glioma cells were a gift from Peter Glazer and grown in high glucose DMEM supplemented with 10% *v/v* FBS. PTEN induction in U251-PTEN

was achieved by the addition of 400 µg/mL G418, 2 µg/mL blasticidin, and 1 µg/mL doxycycline as described elsewhere [9]. PTEN-deficient U87 glioma cells were grown in high-glucose DMEM containing 10% *v/v* FBS.

2.5. Sample preparation

For phospho-53BP1 foci formation and trypan blue exclusion assays, di-scFv variant samples were exchanged into respective growth media (i.e. DMEM or RPMI 1640) and sample concentration was quantified using the Bradford assay. Subsequently, SDS-PAGE with Coomassie staining (Invitrogen) was performed to confirm di-scFv stability in the samples. All samples were filter sterilized using a 0.2 µm pore-sized syringe filter, and the concentration of di-scFv in PBS was quantified using absorbance at 280 nm with a Nanodrop 1000 (Thermo Fisher Scientific).

2.6. In Silico Prediction of Secondary Structure and Disorder Tendency.

Sequence-based prediction of di-scFv secondary and higher order structure was performed using Phyre 2 [11]. To predict short and long-range disorder, sequence data for murine and humanized di-scFv variants E and J was inputted into IUPRED, and the disorder tendency score for each residue was generated [12, 13].

2.7. Circular Dichroism

The secondary structure of murine di-scFv and variants E and J was examined using a Chirascan spectrafluorimeter (Applied Photophysics). Samples analyzed by CD were buffer exchanged into a 10 mM pH 6 potassium phosphate buffer (MWCO 10 kDa) prior to analysis.

Individual CD spectra were collected between 260-190 nm at 20 °C using a 1 mm path length quartz cuvette. A sampling time of one second, step size of 1 nm and bandwidth of 1 nm was used for each measurement. Buffer spectra were also collected using the same data acquisition parameters, and subtracted from sample spectra. The resultant data was converted to molar ellipticity and mean residue ellipticity. Additionally, raw CD data (mdeg) was inputted into CAPITO [14] and BESTSEL [15] to determine the approximate secondary structure content of samples examined.

2.8. Cell penetration assays

DLD-1 cells cultivated in 96-well plates were treated either with control vehicle or 10 µM di-scFv variant(s) for 60 minutes at 37 °C. Subsequently, treated cells were washed with PBS twice, fixed with pre-chilled 100% ethanol. Fixed cells were blocked, incubated with protein L (Invitrogen) and probed with a chicken anti-protein L primary antibody (Invitrogen). Subsequently, cells were treated with an Alexa Fluor 555-conjugated goat anti-chicken antibody (Invitrogen) for one hour at ambient temperature. A DAPI counterstain was applied to aid qualitative assessment of di-scFv localization. All timings and reagents were kept constant for analysis of cell penetration.

2.9. Assessment of phospho-53BP1 (P53BP1) foci formation

In order to assess P53BP1 foci formation, U251 PTEN proficient and deficient cells were cultivated in 96 well plates overnight prior to treatment with di-scFv. Subsequently, cells were treated either with DMEM containing 10 µM di-scFv variant or DMEM (control), and incubated for 24 hours at 37 °C. Following treatment, cells were fixed, blocked, and incubated overnight

with a rabbit anti-P53BP1 primary antibody (Cell signaling technology). Cell monolayers were subsequently probed with an Alexa Fluor 555-conjugated goat anti-rabbit IgG secondary antibody (Life technologies) and counterstained with DAPI prior to image acquisition.

2.10. Image acquisition & data analysis

Cell penetration assays. Images of di-scFv cell penetration were acquired using a Zeiss 710 confocal microscope (Advanced Microscopy Group) using the 543 nm (Alexa Fluor 555) and MaiTai laser (DAPI, blue) lines. Several representative fields of view at a 40X magnification (c-Apochromat 40x/1.2NA water-immersion objective lens) were acquired for each condition. Subsequently, multiple channel images were merged using Image J (NIH, Bethesda, USA). All image acquisition parameters were maintained between samples, and acquired images were deconvoluted in Huygens (version 17.04.1p0). The fluorescence intensity of staining for each cell was analyzed using the Image J (version 1.51n) particle analysis function. Following image thresholding, the fluorescence intensity of each cell was determined and resultant data plotted as box plots in Origin (version b9.4.0.220).

P53BP1 foci. Images were acquired with an EVOS fl digital fluorescence microscope using the DAPI and RFP (red fluorescent protein) filtersets. Several representative fields of view were acquired at a 40X magnification for each treatment and exported as 8-bit TIFF files. The number of foci per cell was determined in Cell Profiler^{TM} (Broad Institute, MA, USA), and only foci co-localized with the DAPI stain were counted.

2.11. Trypan blue exclusion assay

Isogenic BRCA2 proficient and deficient DLD-1 cells, and PTEN-deficient U87 cells were cultivated in 96-well plates and treated with either medium (control), or medium containing 10 μM di-scFv variant. Subsequently, cells were incubated for one week at 37 °C, were assessed using optical microscopy following treatment, trypsinized and treated with trypan blue. Cells were manually counted in a grid, and the number of viable (white) and non-viable (blue) cells quantified.

2.12. Statistical analysis.

All data are represented as mean ±standard error (SEM). Unless otherwise stated, a two-tailed Student's t-test assuming unequal variances was utilized to determine P values and a $P < 0.05$ was deemed as statistically significant.

Results

3.1. Expression of di-scFv variants

Humanized di-scFv 3E10 variants were expressed with varying yields using a modified CHO expression system. Resultant growth medium containing di-scFv variant was subjected to clarification, followed by ion exchange purification. Subsequently, all purified di-scFv was exchanged into pH 7 phosphate-buffered saline and retained for characterization. All di-scFv variants were analyzed by SDS-PAGE. For all lanes, a band corresponding to di-scFv was observed at approximately 54 kDa (see supplementary information, **Figure S1**).

3.2. Analysis of di-scFv variant secondary structure

Following assessment of di-scFv expression and purity in generated stable cell pools, the secondary structure of the variants was predicted using in silico models. Resultant outputs of comparison between di-scFv E, di-scFv J, and the murine prototype are presented (**Figure 1A**). In parallel, CD analysis of these di-scFv fragments was performed (10 mM phosphate buffer, pH 7), to determine whether features of the murine prototype were conserved in the new di-scFv variants (**Figure1B-C**). Evaluation of *in silico* data and rendering of secondary structure suggested no significant change in secondary and higher order structure following humanization of the di-scFvs. This was further confirmed by circular dichroism, with minima evident at 195-200 nm for all di-scFvs. However, in the case of the novel variants, small maxima (positive peak) appeared at approximately 218 nm. Analysis of CD spectra in BESTSEL resulted in assignment of ß-sheet and unassigned secondary structure (consistent with disorder) for all spectra. Similar structural profiles were assigned using CAPITO, albeit with higher NRMSDs. These observations suggest the potential presence of polyproline helices typically associated with intrinsically-disordered or unfolded proteins [16] and are consistent with the proportion of unassigned secondary structure elements (~30%) from the Phyre *in silico* simulations that usually dominate CD spectra [17]. Sequence-based prediction of disorder tendency was further assessed using the IUPRED sequence-based prediction platform [13]. Comparison of output generated from disorder tendency scores for di-scFvs E and J versus murine di-scFv revealed overlap across the sequences examined (**Figure 1D-E**). This suggests that the long- and short-range disorder tendency for these fragments is broadly similar. Overall, evaluation of secondary structure using experimental and in silico data suggested the absence of structural changes following humanization and sequence modification.

Figure 1 placeholder

3.3. Evaluation of nuclear penetration by the di-scFv variants

Previous studies on the cell-penetrating activity of murine (yeast) di-scFv relied on the C-terminal Myc tag for detection. The new variants lacked such tags, and consequently an alternate detection approach was required. Protein L binds most kappa antibody variable domains and was confirmed to aid detection of di-scFv in a western blot (**Figure S2**). Hence, protein L detection was used to compare the abilities of the di-scFv variants to penetrate DLD-1 cell nuclei. Most di-scFv fragments accumulated in cell nuclei, except for di-scFvs I, K and P that were observed to contain limited or no nuclear di-scFv localization. Individual Alexa 555 and DAPI confocal images from protein L immunostaining cells are presented in **Figure 2**. To assess relative heterogeneity of cellular penetration by di-scFv variants, the measured fluorescence intensity obtained from confocal image analysis was plotted for cell populations incubated with each variant (**Figure 2, bottom**). Most variants, except for di-scFvs I, K and P, exhibited significant staining and equivalent profiles in fluorescence intensity.

Figure 2 placeholder

3.4. Di-scFv variants cause accumulation of P53BP1 foci in PTEN-deficient cells

Phosphorylated 53BP1 foci, reporters of DNA double strand breakage (DSB), are transiently observed in normally-dividing cells proficient in DNA damage repair, and are regarded as a mediator of DNA DSB repair [19]. Murine di-scFv was previously shown to cause DSB accumulation in homology-directed repair (HDR)-deficient cancer cells. To assess the impact of

the new di-scFvs on DNA damage, P53BP1 foci accumulation was assessed following a 24 hour incubation with murine (yeast) di-scFv or variants E, G, H, I, J, K, L and M in PTEN-deficient and proficient U251 cells). Example cells from PTEN-proficient and deficient cells and quantification of number of foci per cell are presented in **Figure 3**. For nuclear-penetrating variants (E, G, H, J, L, and M) significant foci accumulation was observed following 24-hours in PTEN-deficient U251 glioblastoma cells (ANOVA, two-tailed, P=0.04). Conversely, in PTEN-expressing cells, no notable difference in P53BP1 foci numbers was observed following treatment (ANOVA, two-tailed, P>0.5). Overall, these data suggest that nuclear-penetrating di-scFv variants retain the ability to inhibit base excision repair (BER) and HDR in PTEN-deficient cells [9]. Variants incapable of localizing to cell nuclei (di-scFvs I and K) did not yield any significant impact on P53BP1 foci, indicating that nuclear penetration is a pre-requisite for foci accumulation.

Figure 3 placeholder

3.5. Di-scFv variants are selectively toxic to cells with deficiencies in DNA damage repair

To establish whether the new variants retain selective toxicity to HDR-deficient cancer cells, matched BRCA2-proficient and deficient DLD-1 cells and PTEN-deficient U87 cells were treated with the murine (yeast) di-scFv and variants G, J, L, and M for seven days, followed by trypan blue exclusion assay to determine the percentage of viable cells. Brightfield micrographs captured prior to trypan blue staining revealed prominent changes in cell morphology and a lack of proliferation for treated BRCA2-deficient cells, but BRCA2-proficient cells were unaffected by treatment (**Figure 4A**). Analysis of cell viability demonstrated that di-scFv variants were

toxic to BRCA2-deficient DLD-1 cells (**Figure 4B**) and PTEN-deficient U87 cells (**Figure 4C**) when compared to control, but not to BRCA2-proficient DLD-1 cells.

Figure 4 placeholder

4. Discussion

A combination of advancements in antibody characterization, novel linker chemistries, and fine-tuning of antibody fragments has opened the door to re-engineering of cell-penetrating autoantibodies capable of bypassing biological barriers to tumor drug delivery. Cell-penetrating autoantibodies exemplified by DNA-damaging autoantibody, 3E10, are compelling candidates for further development. 3E10 preferentially localizes to tumors *in vivo* and exerts single-agent effects on DNA repair-deficient cancer cells, while sparing normal cells. However, it has previously been unknown whether 3E10 would retain its key functionality once humanized for clinical development. We have demonstrated the successful design and expression of humanized di-scFvs, and found that most have equivalent or enhanced activity relative to the yeast murine di-scFv prototype.

The di-scFv variants were subjected to a functional assay cascade beginning with an evaluation of cell penetration ability. Most di-scFv variants exhibited nuclear localization, except for di-scFvs I, K, and P that demonstrated limited or no nuclear staining in DLD-1 cells and were subsequently found to have no significant impact on P53BP1 foci accumulation. Intriguingly, broader heterogeneity in nuclear penetration was observed with some variants in comparison to others as represented in population data (**Figure 2**). Observed differences in maximum staining

intensity across the panel of variants examined may be related to differential affinity for DNA and exploitation of ENT2 transporter trafficking [20]. An assessment of the mechanism of cell penetration is outside the scope of the present work, and further studies are required to elucidate the sequence of events leading to internalization and trafficking of 3E10 to cell nuclei.

To confirm that the di-scFv variants exhibited similar or enhanced effects on DSB accumulation (P53BP1 foci) relative to murine di-scFv, U251 cells (PTEN proficient and deficient) were treated with a select panel of di-scFv variants for 24 hours. Consistent with previous observations reported by Noble et al [9] on the yeast murine di-scFv, significant accumulation of DSBs was found in the treated PTEN-deficient cells, and no DSB accumulation was observed in PTEN-proficient cells.

Murine di-scFv expressed in yeast has previously been shown to be synthetically lethal to HDR-deficient cancer cells but to spare cells with intact HDR [9]. Due to limitations relating to quantities of di-scFv variants available for initial testing, screens for toxicity to BRCA2- and PTEN-deficient cancer cells were performed in a small scale 96-well format trypan blue exclusion assay. Future evaluation of lead candidates and other novel di-scFvs will include automated cell proliferation assays and clonogenic assessment of cell survival over various incubation periods in additional cell lines with known HDR defects.

In silico sequence-based prediction of secondary structure revealed no significant changes between the novel di-scFv variants and the murine (yeast) prototype. In all cases, an unassigned or disordered secondary structure proportion (up to 40%) was observed in variants examined. Further assessment of the sequence, using IUPRED short- and long-range disorder tendency prediction, yielded overlapping profiles for the di-scFvs examined. CD analysis of di-scFv samples indicated a similar overall profile shape, with the presence of minima at 195-200 nm

(**Figure 1**). In the case of humanized variants, a small maximum was observed at 218 nm. Observed differences in molar ellipticity may be attributed to differences in analyte monomeric purity rather than structural differences. Overall, *in silico* and CD analyses indicate the presence of some ß-sheet structure consistent with antibodies, and disorder associated with unassigned *in silico* allocations and CD spectra.

Intrinsically-disordered proteins (IDPs) exist in conformationally-flexible states lacking 3D structure under native physiological conditions. A more in-depth analysis of the molecular machinery implicated in the trafficking of 3E10 to the nucleus and ligand binding studies are required to understand processes that confer functionality to 3E10. Understanding such structural determinants may shed light on the pathophysiology of cell-penetrating autoantibodies, aid target discovery for SLE, and contribute to the design of effective targeting sequences.

In conclusion, we have demonstrated the successful humanization of 3E10-derived di-scFv fragments with conserved structural properties and equivalent or enhanced *in vitro* activity, with a view to developing novel therapeutics against HDR-deficient tumors. This work has led to the selection of a lead candidate for progression to pre-clinical development. Further work is underway to evaluate *in vivo* efficacy of these antibodies as monotherapies in tumor-bearing models and their potential as targeting ligands for nuclear drug delivery.

Acknowledgements

This study was supported by Patrys Ltd.

Conflict of Interest

ZR, VD, JAC, and JEH are inventors on the IP related to 3E10 variants described in this work. VD, DLG, JAC and JEH have equity interest in Patrys Ltd. VD, DLG, and JAC are employees of Patrys Ltd.

Author Contributions

V.D., D.L.G. and J.A.C., and J.E.H initiated the study. N.R., V.D., D.L.G., C.H.J., and J.A.C. contributed to study design and analyzed data. Z.R. and J.E.H. designed, performed experiments and analyzed the data. The manuscript was written by Z.R. and J.E.H and reviewed by all authors.

References

[1] P. Polakis, Antibody Drug Conjugates for Cancer Therapy, Pharmacological Reviews, 68 (2016) 3-19.

[2] I.-K. Choi, R. Strauss, M. Richter, C.-O. Yun, A. Lieber, Strategies to Increase Drug Penetration in Solid Tumors, Frontiers in Oncology, 3 (2013) 193.

[3] A.M. Scott, J.D. Wolchok, L.J. Old, Antibody therapy of cancer, Nat Rev Cancer, 12 (2012) 278-287.

[4] P.W. Noble, S. Bernatsky, A.E. Clarke, D.A. Isenberg, R. Ramsey-Goldman, J.E. Hansen, DNA-damaging autoantibodies and cancer: the lupus butterfly theory, Nat Rev Rheumatol, 12 (2016) 429-434.

[5] L. Rivadeneyra-Espinoza, A. Ruiz-Argüelles, Cell-penetrating anti-native DNA antibodies trigger apoptosis through both the neglect and programmed pathways, Journal of Autoimmunity, 26 (2006) 52-56.

[6] R.H. Weisbart, M. Stempniak, S. Harris, D.J. Zack, K. Ferreri, An Autoantibody is Modified for Use as a Delivery System to Target the Cell Nucleus: Therapeutic Implications, Journal of Autoimmunity, 11 (1998) 539-546.

[7] R.H. Weisbart, G. Chan, G. Jordaan, P.W. Noble, Y. Liu, P.M. Glazer, R.N. Nishimura, J.E. Hansen, DNA-dependent targeting of cell nuclei by a lupus autoantibody, Scientific Reports, 5 (2015) 12022.

[8] J.E. Hansen, G. Chan, Y. Liu, D.C. Hegan, S. Dalal, E. Dray, Y. Kwon, Y. Xu, X. Xu, E. Peterson-Roth, E. Geiger, Y. Liu, J. Gera, J.B. Sweasy, P. Sung, S. Rockwell, R.N. Nishimura, R.H. Weisbart, P.M. Glazer, Targeting cancer with a lupus autoantibody, Science translational medicine, 4 (2012) 157ra142-157ra142.

[9] P.W. Noble, G. Chan, M.R. Young, R.H. Weisbart, J.E. Hansen, Optimizing a Lupus Autoantibody for Targeted Cancer Therapy, Cancer Research, 75 (2015) 2285-2291.

[10] Z. Chen, J.M. Patel, P.W. Noble, C. Garcia, Z. Hong, J.E. Hansen, J. Zhou, A lupus anti-DNA autoantibody mediates autocatalytic, targeted delivery of nanoparticles to tumors, 2016.

[11] L.A. Kelley, S. Mezulis, C.M. Yates, M.N. Wass, M.J.E. Sternberg, The Phyre2 web portal for protein modeling, prediction and analysis, Nat. Protocols, 10 (2015) 845-858.

[12] B. Mészáros, I. Simon, Z. Dosztányi, Prediction of Protein Binding Regions in Disordered Proteins, PLOS Computational Biology, 5 (2009) e1000376.

[13] Z. Dosztányi, B. Mészáros, I. Simon, ANCHOR: web server for predicting protein binding regions in disordered proteins, Bioinformatics, 25 (2009) 2745-2746.

[14] C. Wiedemann, P. Bellstedt, M. Görlach, CAPITO—a web server-based analysis and plotting tool for circular dichroism data, Bioinformatics, 29 (2013) 1750-1757.

[15] A. Micsonai, F. Wien, L. Kernya, Y.-H. Lee, Y. Goto, M. Réfrégiers, J. Kardos, Accurate secondary structure prediction and fold recognition for circular dichroism spectroscopy, Proceedings of the National Academy of Sciences, 112 (2015) E3095-E3103.

[16] A. Rodger, Far UV Protein Circular Dichroism, in: G.C.K. Roberts (Ed.) Encyclopedia of Biophysics, Springer Berlin Heidelberg, Berlin, Heidelberg, 2013, pp. 726-730.

[17] J.L.S. Lopes, A.J. Miles, L. Whitmore, B.A. Wallace, Distinct circular dichroism spectroscopic signatures of polyproline II and unordered secondary structures: Applications in secondary structure analyses, Protein Science : A Publication of the Protein Society, 23 (2014) 1765-1772.

[18] Z. Dosztányi, V. Csizmók, P. Tompa, I. Simon, The Pairwise Energy Content Estimated from Amino Acid Composition Discriminates between Folded and Intrinsically Unstructured Proteins, Journal of Molecular Biology, 347 (2005) 827-839.

[19] A. Gupta, C.R. Hunt, S. Chakraborty, R.K. Pandita, J. Yordy, D.B. Ramnarain, N. Horikoshi, T.K. Pandita, Role of 53BP1 in the Regulation of DNA Double-Strand Break Repair Pathway Choice, Radiation research, 181 (2014) 1-8.

[20] J.E. Hansen, C.-M. Tse, G. Chan, E.R. Heinze, R.N. Nishimura, Weisbart, Richard H., Intranuclear Protein Transduction through a Nucleoside Salvage Pathway, Journal of Biological Chemistry, 282 (2007) 20790-20793.

Figure Legends

Figure 1 *In silico renditions* of Phyre predicted structures for di-scFv in Jmol **(A)**, corresponding molar ellipticity, **(B)** mean residue ellipticity measured by far UV circular dichroism **(C)**, and IUPRED in silico predictions of long **(D)** and short-range **(E)** predicted disorder tendency [18].

Figure 2 Cellular penetration assay of di-scFv variants and corresponding box plots. DLD-1 cells were treated with either control vehicle or 10 μM di-scFv variant. Following treatment, cells were immunostained with protein L, anti-protein L primary antibody and an Alexa Fluor 555 conjugated secondary antibody (and a DAPI counterstain). Box plots represent nuclear fluorescence intensity determined from the analysis of corresponding confocal images. ● represents the mean intensity, and the horizontal box lines represent the median, lower and upper quartiles. The whiskers represent outliers.

Figure 3 Di-scFv variants cause accumulation of DSBs in PTEN-deficient U251 cells. Treatment with di-scFv variants resulted in accumulation of phospho-53BP1 foci (pink) in PTEN-deficient U251 cells (blue, DAPI counterstain). Mean number of measured P53BP1 foci per cell determined following treatment with di-scFv variants (top), and example U251-PTEN (upper bottom panel) and U251 (lower bottom panel) cell images following a 24 hour incubation with 10 μM di-scFv variants as visualized by immunofluorescence. PTEN-deficient U251 cells demonstrate an accumulation in P53BP1 foci following treatment with di-scFv variants.

Figure 4 Di-scFv variants are toxic to HDR-deficient cancer cells. A representative field of view of DLD-1 parental and BRCA 2- deficient cells following treatment with RMPI (control) or 10 μM di-scFv_G for seven days **(A)**. Percent viability relative to control, measured by trypan blue exclusion, for BRCA2-proficient and deficient DLD-1 cells **(B)** and PTEN-deficient U87 cells incubated with selected di-scFv variants for seven days **(C)**.

Figure 1

Click here to download high resolution image

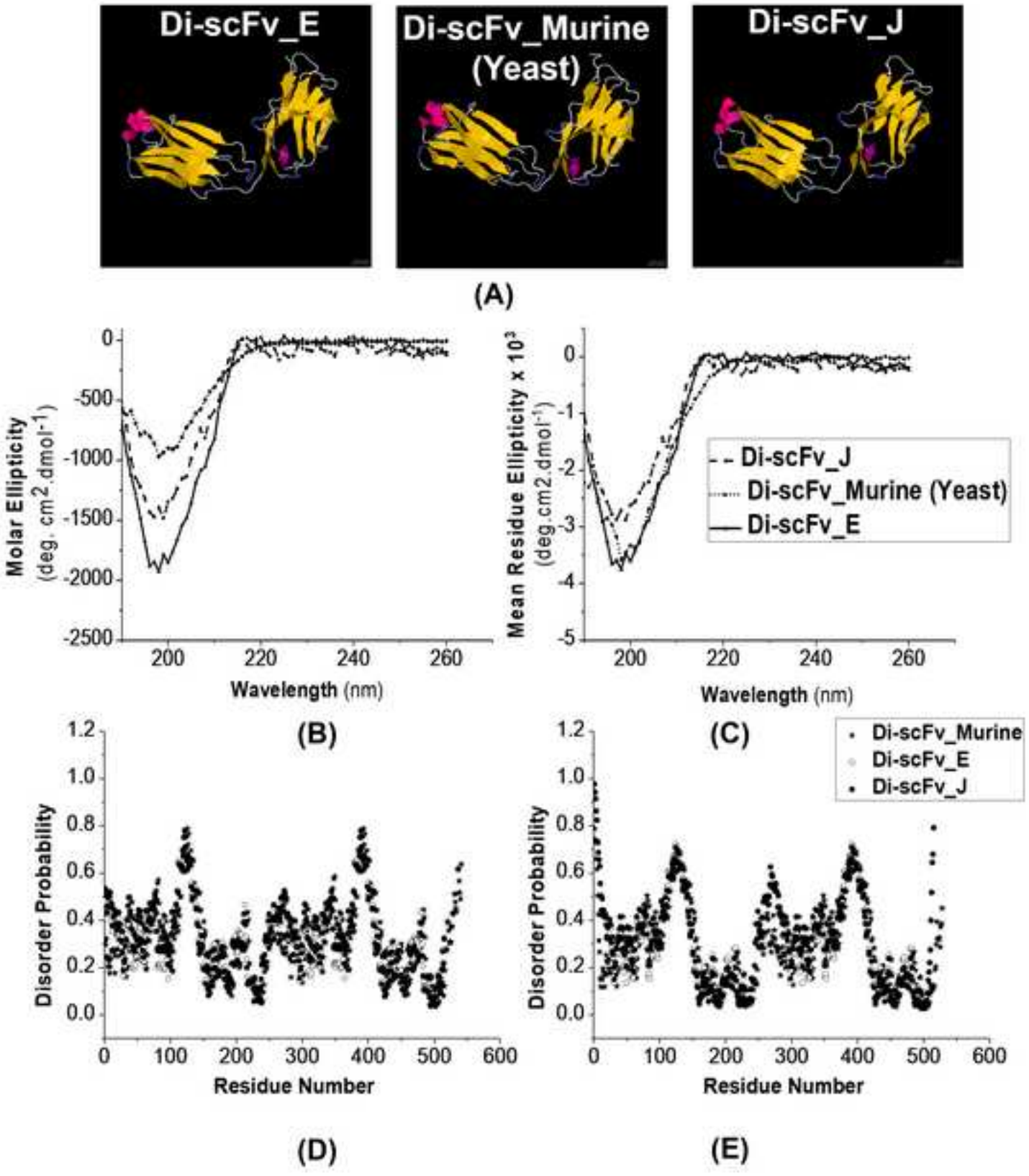

Figure 2

Click here to download high resolution image

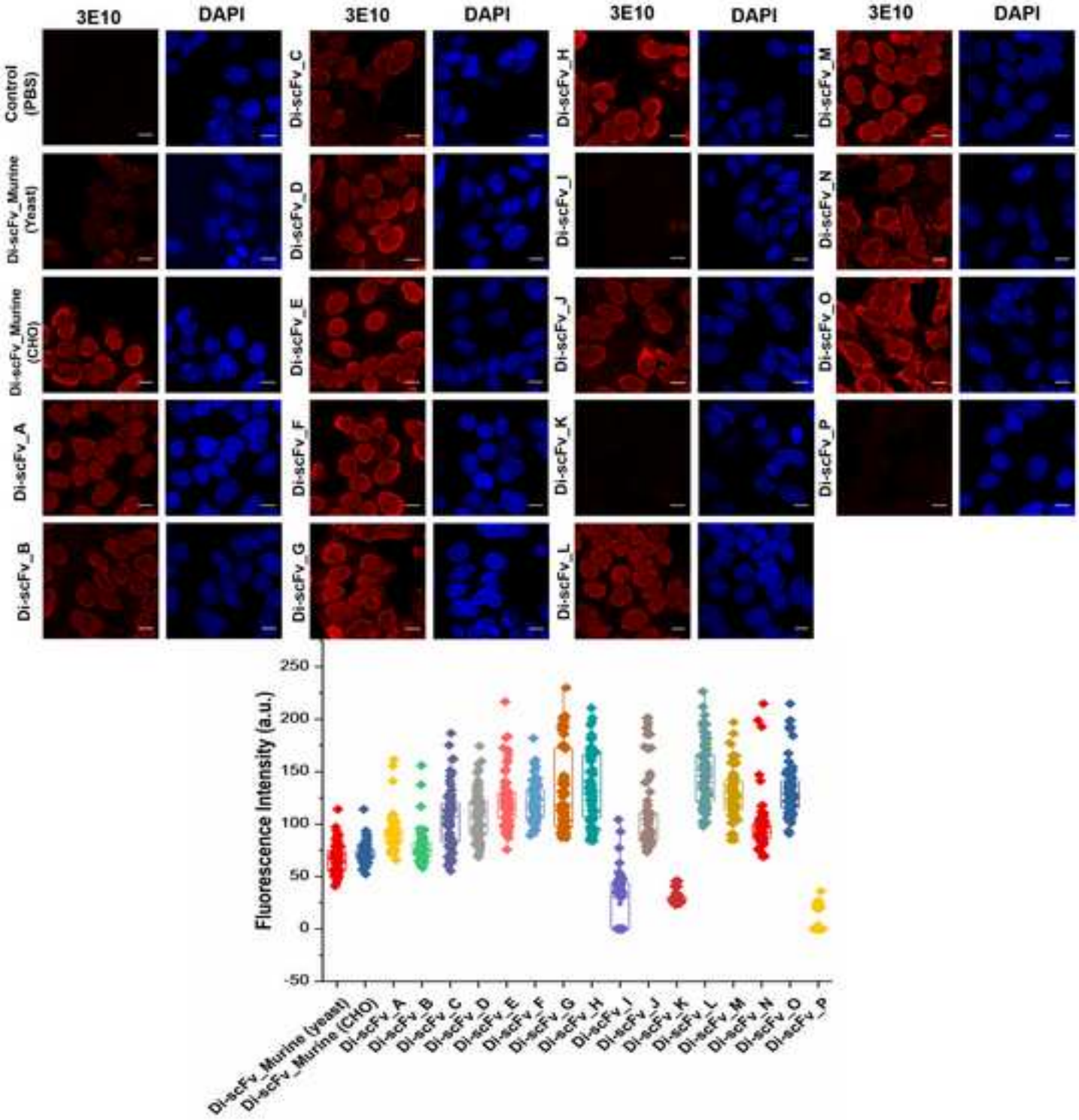

Figure 3

Click here to download high resolution image

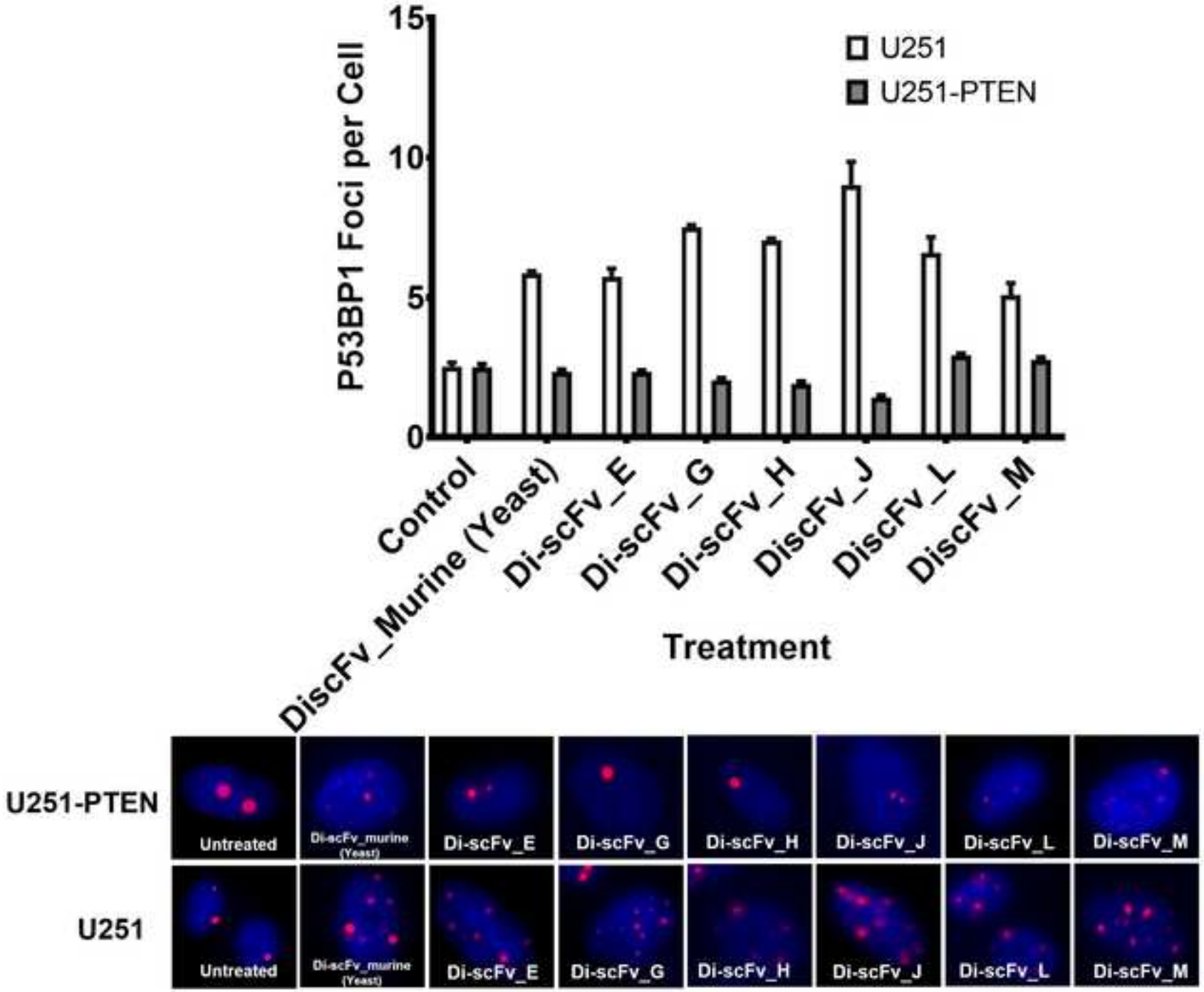

Figure 4
Click here to download high resolution image

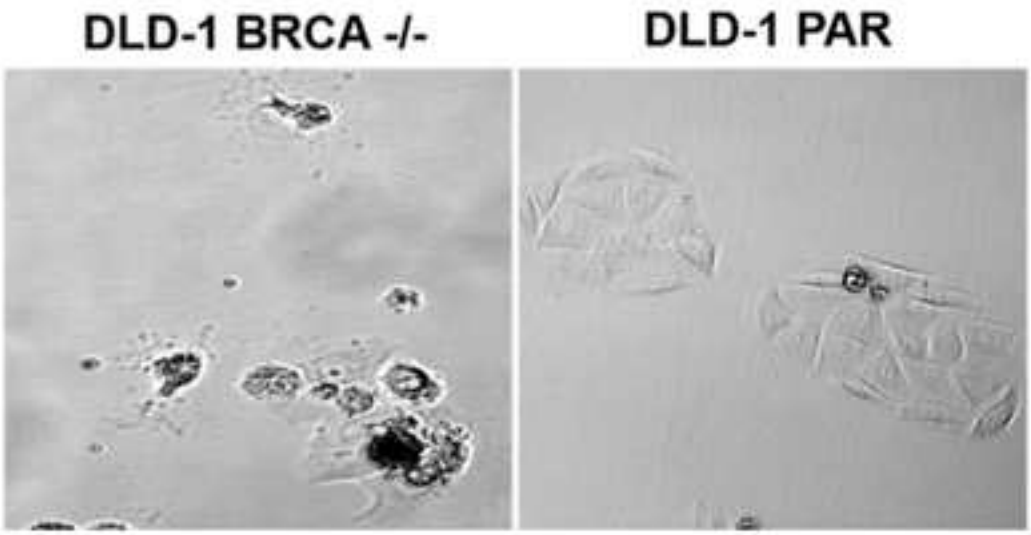

(A)

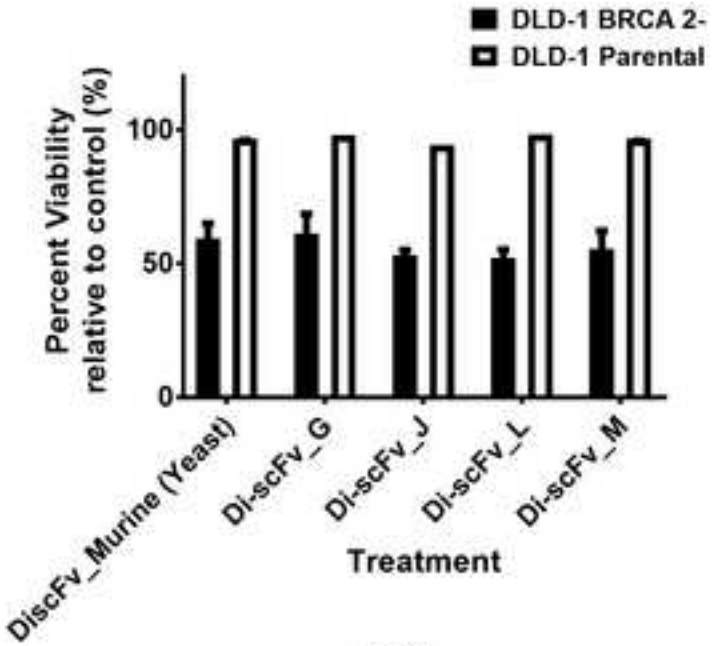

(B)

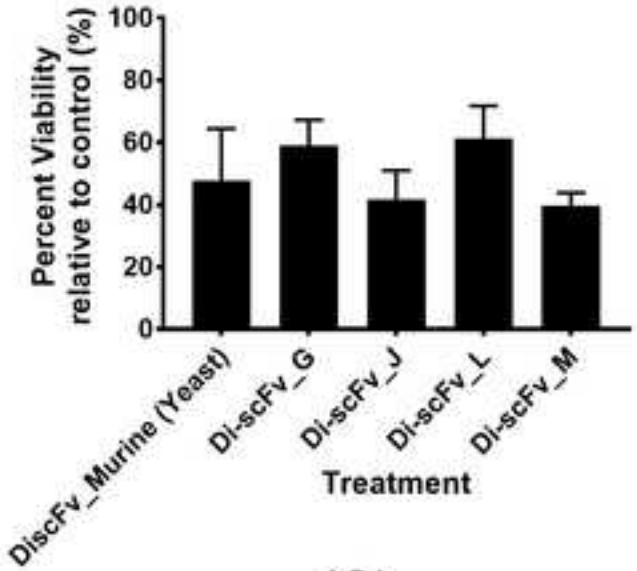

(C)

Electronic Supplementary Material (online publication only)

Click here to download Electronic Supplementary Material (online publication only): Supplementary information_FINAL.docx

***Conflict of Interest**

Please wait...

If this message is not eventually replaced by the proper contents of the document, your PDF viewer may not be able to display this type of document.

You can upgrade to the latest version of Adobe Reader for Windows®, Mac, or Linux® by visiting http://www.adobe.com/go/reader_download.

For more assistance with Adobe Reader visit http://www.adobe.com/go/acrreader.

***Conflict of Interest**

Please wait...

If this message is not eventually replaced by the proper contents of the document, your PDF viewer may not be able to display this type of document.

You can upgrade to the latest version of Adobe Reader for Windows®, Mac, or Linux® by visiting http://www.adobe.com/go/reader_download.

For more assistance with Adobe Reader visit http://www.adobe.com/go/acrreader.

***Conflict of Interest**

Please wait...

If this message is not eventually replaced by the proper contents of the document, your PDF viewer may not be able to display this type of document.

You can upgrade to the latest version of Adobe Reader for Windows®, Mac, or Linux® by visiting http://www.adobe.com/go/reader_download.

For more assistance with Adobe Reader visit http://www.adobe.com/go/acrreader.

***Conflict of Interest**

Please wait...

If this message is not eventually replaced by the proper contents of the document, your PDF viewer may not be able to display this type of document.

You can upgrade to the latest version of Adobe Reader for Windows®, Mac, or Linux® by visiting http://www.adobe.com/go/reader_download.

For more assistance with Adobe Reader visit http://www.adobe.com/go/acrreader.

***Conflict of Interest**

Please wait...

If this message is not eventually replaced by the proper contents of the document, your PDF viewer may not be able to display this type of document.

You can upgrade to the latest version of Adobe Reader for Windows®, Mac, or Linux® by visiting http://www.adobe.com/go/reader_download.

For more assistance with Adobe Reader visit http://www.adobe.com/go/acrreader.

***Conflict of Interest**

Please wait...

If this message is not eventually replaced by the proper contents of the document, your PDF viewer may not be able to display this type of document.

You can upgrade to the latest version of Adobe Reader for Windows®, Mac, or Linux® by visiting http://www.adobe.com/go/reader_download.

For more assistance with Adobe Reader visit http://www.adobe.com/go/acrreader.

***Conflict of Interest**

Please wait...

If this message is not eventually replaced by the proper contents of the document, your PDF viewer may not be able to display this type of document.

You can upgrade to the latest version of Adobe Reader for Windows®, Mac, or Linux® by visiting http://www.adobe.com/go/reader_download.

For more assistance with Adobe Reader visit http://www.adobe.com/go/acrreader.